ACS OMEGA

http://pubs.acs.org/journal/acsodf

Article

Improved Stability of Human CGI-58 Induced by Phosphomimetic S237E Mutation

Miriam Livier Llamas-García, Edgar D. Páez-Pérez, Claudia G. Benitez-Cardoza, Gabriela M. Montero-Morán,* and Samuel Lara-González*

Cite This: *ACS Omega* 2022, 7, 12643−12653

Read Online

ACCESS | Metrics & More | Article Recommendations | Supporting Information

ABSTRACT: In lipolysis, the activating function of CGI-58 is regulated by its interaction with perilipin 1 (PLIN1) localized on the lipid droplet (LD), and its release is controlled by phosphorylation. Once lipolysis is stimulated by catecholamines, protein kinase A (PKA)-mediated phosphorylation enables the dissociation of the CGI-58/PLIN1 complex, thereby recruiting adipose triglyceride lipase (ATGL) and hormone-sensitive lipase (HSL) to initiate fatty acid release. It has been shown that mouse CGI-58 mutant S239E, which mimics the phosphorylation of this residue, is able to dissociate from the CGI-58/PLIN1 complex and activate ATGL. Here, we analyze the stabilizing effect on human CGI-58 of a triple tryptophan to alanine mutant (3WA) on the LD-binding motif, as well as a quadruple mutant in which the phosphomimetic S237E substitution was introduced to the 3WA construct (3WA/S237E). We found that tryptophan residues promote wild-type (WT) protein aggregation in solution since their substitution for alanine residues favors the presence of the monomer. Our experimental data showed increased thermal stability and solubility of 3WA/S237E protein compared to the 3WA mutant. Moreover, the 3WA/S237E protein showed proper folding and a functional binding site for oleoyl-CoA. The analysis of a bioinformatic three-dimensional (3D) model suggests an intramolecular interaction between the phosphomimetic glutamic acid and a residue of the α/β hydrolase core. This could explain the increased solubility and stability observed in the 3WA/S237E mutant and evidences the possible role of serine 237 phosphorylation.

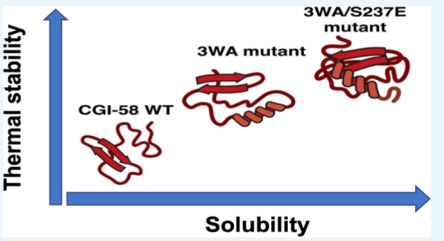

1. INTRODUCTION

The CGI-58 (Comparative Gene Identification-58) protein was identified in a study in which the proteome of *Caenorhabditis elegans* was compared against a database of human expressed sequence tags (ESTs), revealing that it is widely expressed in various tissues, including skin, lymphocytes, liver, skeletal muscle, and brain tissue.[1] It belongs to the α/β hydrolase family, which is characterized by a catalytic triad formed by a nucleophile, an acid, and a histidine residue. However, CGI-58 differs from the other members of the family in which it contains a residue of asparagine instead of the serine nucleophile; therefore, it has no hydrolase activity. In the human protein, the catalytic triad is formed by N153, H327, and D301 or E177.[2,3] The relevance of CGI-58 in lipid metabolism was recognized in 2001 when it was found that mutations in its gene (deletions, insertions, and point mutations at residues 7, 33, 130, and 260) cause a neutral lipid storage disease called Chanarin−Dorfman syndrome (CDS). Nineteen years later, more than 40 different mutations have been reported across the entire protein sequence with no specific localization.[4] CDS is characterized by the presence of ichthyosis and the intracellular accumulation of lipid droplets (LD) in various tissues.[2]

It is currently known that CGI-58 is involved in the regulation of different metabolic and tissue-specific signaling pathways through interaction with other proteins.[4] Lipolysis in white adipose tissue is the metabolic process in which CGI-58 has been shown to be an essential factor in activating the adipose triglyceride lipase (ATGL), the enzyme that initiates triacylglycerol (TAG) hydrolysis. In mice, CGI-58 increases the activity of ATGL up to 20 times by making direct protein−protein interaction; however, the interaction region is largely unknown. It has recently been shown that the activation process involves the C-terminal region of CGI-58, and in particular, the R299 and G328 residues have been reported as essential.[5−7] In addition to increasing its activity, CGI-58 extends the regioselectivity of ATGL to the *sn*-1 position of the fatty acid. Thus, in the presence of CGI-58, ATGL generates *sn*-1,3 and *sn*-2,3 diacylglycerol, which allows higher rates of lipolysis and increases the release of fatty acids for energy production.[8] The lipase-activating function of CGI-58 is regulated by its binding to perilipin 1 (PLIN1), a peripheral protein that restricts the access of cytosolic lipases to TAG stored within the LD,[9] and its release is controlled by phosphorylation. Under basal conditions, CGI-58 interacts

Received: December 4, 2021
Accepted: March 22, 2022
Published: April 5, 2022

https://doi.org/10.1021/acsomega.1c06872
ACS Omega 2022, 7, 12643−12653

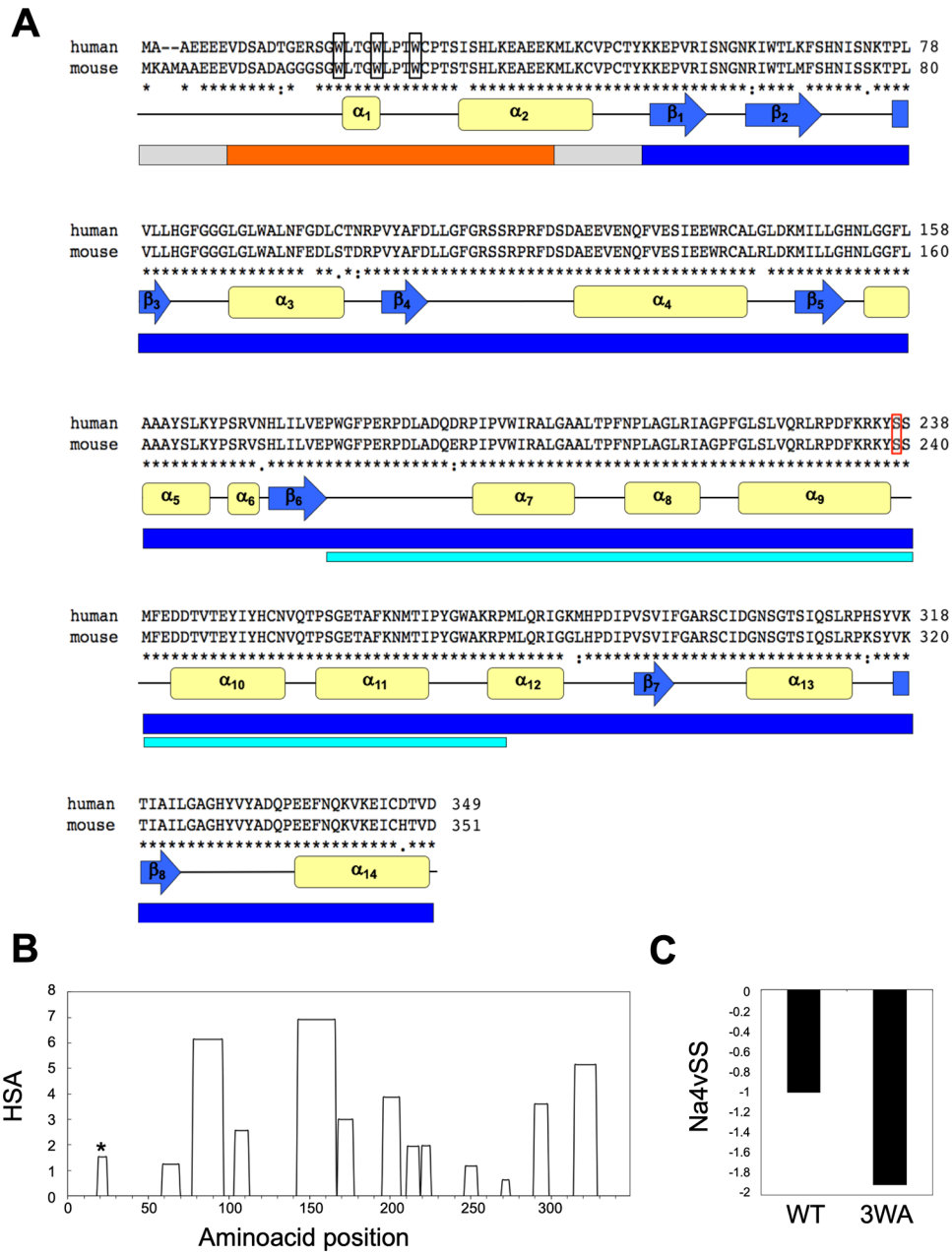

Figure 1. Bioinformatic analysis and structural properties of CGI-58. (A) Amino acid sequence alignment of human (Q8WTS1.1) and mouse (Q9DBL9.1) CGI-58 is shown on top, tryptophan residues involved in LD binding (W19, W23, and W27) are shown enclosed in black squares, while the phosphorylation site comprising residue S237 is enclosed in a red square; the alignment was performed with the T-Coffee Multiple Sequence Alignments Tool. Below the alignment, the secondary structure prediction of human CGI-58 performed using the JPred4 and PredicProtein web servers is shown; α-helices are represented by yellow rectangles, while blue arrows show β-strands. At the bottom, domain elements of CGI-58 are shown: the LD-binding region is orange (residues 8−41), the α/β hydrolase core is blue (residues 52−349), and the active site cap is cyan (residues 178−276). (B) Aggregation prediction analysis, the hotspot area (HSA) plot for the CGI-58 amino acid sequence is shown. The hotspot marked with * is lost in the 3WA mutant. (C) Normalized aggregation propensity values (Na4vSS) estimated for the WT and 3WA amino acid sequences are shown. Low aggregation propensity is expected with lower negative values, while positive values suggest higher aggregation propensity. Data analysis was performed using the AGGRESCAN web server.

with the C-terminal end of PLIN1 and remains attached to the LD of the adipocyte through the tryptophan residues at its N-terminal end (W21, W25, W29, of mouse protein). The N-terminal region is an extension of the hydrolase structural domain of the protein, which is mainly unstructured and has been proposed as an independent LD anchor.[6,10] Upon β-adrenergic stimulation, cAMP-dependent protein kinase A (PKA) phosphorylates as many as six serine residues in PLIN1 and serine 239 of the KYSS motif in mouse CGI-58 (residue 237 in human protein), resulting in the release of CGI-58 from PLIN1 and allowing CGI-58 to recruit ATGL to the LD.[9,11,12] A recent study reported two synthetic compounds that bind to CGI-58 and disrupt the interaction with PLIN1, bypassing the PKA signaling pathway. Interestingly, Y330 was found in the binding pocket, which also binds oleoyl-CoA.[13]

Despite the relevance of tryptophan residues from the N-terminal end and the phosphorylation of the serine residue in the regulation of lipolysis, the functional role of these residues

https://doi.org/10.1021/acsomega.1c06872
ACS Omega 2022, 7, 12643−12653

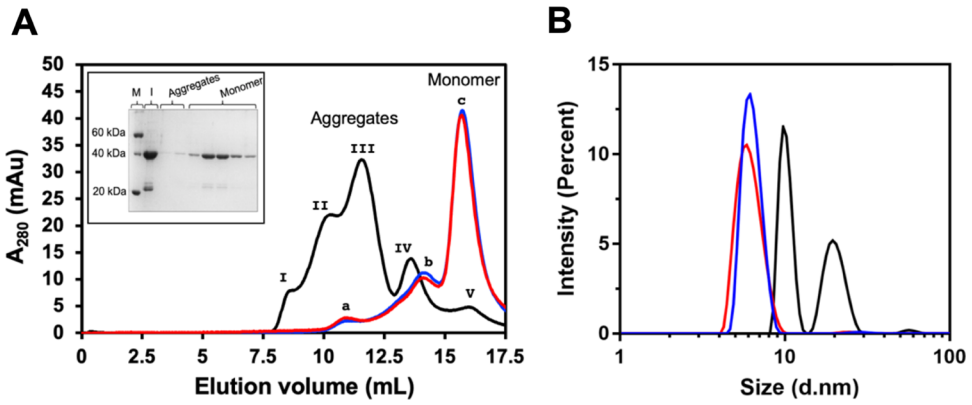

Figure 2. Size-exclusion chromatograms and dynamic light scattering (DLS) analyses of CGI-58 WT, 3WA, and 3WA/S237E. (A) SEC elution profiles of CGI-58 WT, 3WA, and 3WA/S237E proteins separated in a Superdex-200 column; purification was done under identical conditions. Elution peaks for the monomer and aggregates are indicated. I, ND; II, 644.7; III, 314.8; IV, 107.4; V, 31.1; a, 441.1; b, 82.5; and c, 37.6 kDa. Black line, WT; blue line, 3WA; red line, 3WA/S237E. The inset shows the sodium dodecyl sulfate-polyacrylamide gel electrophoresis (SDS-PAGE) analysis of 3WA/S237E purified fractions (red line); the gel was visualized by coomassie blue staining. M, protein weight markers; I, protein sample loaded to the column; aggregates, peaks a and b; monomer, elution fractions from 15 to 17.5 mL. (B) Monomer fractions shown in panel (A) were collected and analyzed by dynamic light scattering. The WT protein (black line) showed two peaks, with diameter particle sizes of 10.2 ± 0.4 and 19.5 ± 2.5 nm. The estimated diameter particle sizes of 3WA (blue line) and 3WA/S237E (red line) were 6.6 ± 0.8 and 6.4 ± 1.0 nm, respectively, which approximate the molecular weights of the monomers (55.7 ± 15.8 kDa and 55.8 ± 14 kDa, respectively); both proteins display a single monodisperse peak. Representative experiments are shown in (A) and (B).

in CGI-58 is not known in detail. Therefore, in this work, we analyzed the impact of the replacement of the N-terminal tryptophan by alanine residues by generating a triple mutant (3WA), as well as the introduction of phosphomimetic mutation S237E to the 3WA triple construct (3WA/S237E) to evaluate their role in the structural and physicochemical properties of the human CGI-58 protein. Our biochemical and biophysical results suggest that tryptophan residues at the N-terminus function as an aggregation nucleation site. For the quadruple 3WA/S237E mutant, our findings showed increased thermal stability and solubility with proper folding and a functional binding site for oleoyl-CoA. The positive contribution of the phosphomimetic mutation S237E could be explained by a putative intramolecular interaction between the glutamic acid and a residue in the α/β hydrolase core.

RESULTS AND DISCUSSION

CGI-58 Contains an Aggregation Hotspot at the N-Terminal Region. Human CGI-58 consists of a sequence of 349 amino acid residues with a theoretical mass of 39.1 kDa. The protein contains an independent LD-binding motif at the N-terminus and a structural domain belonging to the α/β hydrolases described in Figure 1A. As can be seen, it shares characteristics with its mouse ortholog as there is a 94% identity between both proteins. For instance, the structural domain formed by residues 52−349 (shown in blue in Figure 1A) consists of the α/β hydrolase fold with a β-sheet in the core of the protein containing 8 β-strands surrounded by 2 and 4 α-helices on each side.[3] Residues 178−276 (cyan in Figure 1A) are considered an insertion to the α/β hydrolase core, which shows a propensity to form α-helix type structures (α_6−α_{11}), and have been proposed to function as a cap that protects the potential catalytic site from direct access to the surface.[3] The LD-binding motif is an extension of the structural domain, which is located at the N-terminal end and comprises residues 10−43. This motif is characterized by the presence of tryptophan residues 19, 23, and 27, which act as a binding anchor to the LD and are necessary for ATGL activation; following these three residues, there is a flexible region (residue 30−38) that allows orientation without restrictions of the α/β hydrolase domain.[6,10]

The amino acid sequence analysis for human CGI-58 using the AGGRESCAN server enabled the identification of 13 possible aggregation hotspots (Figure 1B). These sites have been described as short and specific sequences of amino acids that function as nucleation points in the aggregation process.[14] Twelve of the thirteen possible hotspots identified are distributed along the structural domain of CGI-58 between residues 52 and 349 and are therefore hidden in the protein core participating in the contact network that stabilizes the protein. This kind of distribution has been proposed as a protective mechanism against aggregation in globular proteins.[14] Interestingly, the first hotspot in the sequence, comprising residues 19−25, fulfills the characteristics of a true hotspot since it is exposed to the solvent and located in an unstructured region; therefore, it could function as an aggregation nucleation site. The amino acid composition of this region shows residues with a high propensity to form aggregates, such as the leucine residues at positions 20 and 24 and the three tryptophan residues at positions 19, 23, and 27.[15] Considering this information, along with the role of the three tryptophan residues in lipid drop binding,[6,10] we decided to generate the triple mutant W19A/W23A/W27A (3WA) to analyze and examine the role of this region in CGI-58 stability. It is worth mentioning that the sequence analysis of the triple 3WA mutant on the AGGRESCAN server shows the elimination of the hotspot in residues 19−25. In addition, the average aggregation propensity value (Na4vSS) calculated by AGGRESCAN was −1.0 for the CGI-58 wild-type (WT) protein and −1.9 for the 3WA mutant (Figure 1C), suggesting higher solubility for the mutant protein.[16]

Triple Mutant 3WA and Phosphomimetic Substitution of S237 Promote the Monomeric State and Solubility of CGI-58. The CGI-58 WT protein and the 3WA mutant were subjected to purification assays along with a quadruple mutant in which serine 237 of the 3WA construct

https://doi.org/10.1021/acsomega.1c06872
ACS Omega 2022, 7, 12643−12653

was substituted by glutamic acid (3WA/S237E). We decided to analyze the role of S237E mutation as a previous report showed that the phosphomimetic substitution of serine 239 for glutamic acid in mouse CGI-58 resulted in a protein with enhanced solubility.[12,17] Initial attempts to purify CGI-58 WT resulted in very low protein yield, which could not be improved even when evaluating different conditions such as temperature, expression time, and expression strains. To circumvent this situation, the 3WA protein was purified, and the thermal stability of the protein in the presence of several additives was analyzed by a fluorescence-based thermal displacement assay.[18] As a result, the composition of an optimized buffer was defined; this buffer was used to purify CGI-58 WT, 3WA, and 3WA/S237E proteins.

The experimental data from the purification by size-exclusion chromatography (SEC) of CGI-58 WT, 3WA, and 3WA/S237E are shown in Figure 2A; the three proteins were purified under the same conditions. The elution profile of the WT protein (Figure 2A, black line) resulted in a heterogeneous population showing that the protein mainly elutes as aggregates of different molecular weights (107.4, 314.8, and 644.7 kDa) with a small fraction of the monomer (31.0 kDa). In contrast, the 3WA protein showed a less heterogeneous profile with two main peaks, of which the peak of the monomer showed ∼5 times higher absorbance than the peak of the aggregates (Figure 2A, blue line). Similarly, the 3WA/S237E mutant showed the same profile observed for the 3WA with almost identical absorbance, as the total protein loaded to the column was the same as that of 3WA and CGI-58 WT. The inset of Figure 2A shows the electrophoretic profile of 3WA/S237E purified fractions under denaturing conditions. As can be seen, the 3WA/S237E protein elutes primarily as a monomer; similar results were observed for the 3WA protein.

After SEC purification, the monomer fractions of CGI-58 WT, 3WA, and 3WA/S237E were further analyzed by dynamic light scattering (DLS) to gain more insights into their hydrodynamic properties (Figure 2B). Interestingly, the monomer fraction of the CGI-58 WT protein showed a high tendency to aggregate, as DLS analysis showed two peaks with particle sizes of 10.2 ± 0.4 and 19.5 ± 2.5 nm diameter, which corresponds to estimated molecular weights of 156.5 ± 9.5 and 697.2 ± 102.9 kDa, respectively. On the contrary, the 3WA mutant showed a single monodisperse peak with a diameter particle size of 6.6 ± 0.8 nm, which approximates the molecular weight of the monomer (55.7 ± 15.8 kDa). Similarly, the 3WA/S237E mutant also displayed a single monodisperse peak with the molecular weight of the monomer (diameters of 6.4 ± 1.0 nm and 55.8 ± 14 kDa). These results suggest that tryptophan residues 19, 23, and 27 may be involved in the aggregation process of the CGI-58 WT protein, as the strong tendency to aggregate observed for the protein after SEC purification was not observed in the 3WA or 3WA/S237E mutants. Moreover, the experimental results agree with the AGGRESCAN analysis, according to which residues 19−25 are predicted as an aggregation hotspot that confers a higher aggregation propensity to the WT protein. The N-terminal region is essential for CGI-58 localization to LD. It was proposed to be an independent functional motif since when yellow fluorescent protein was fused to residues 19−35, the fusion protein localizes to LDs. Moreover, structural analysis of a peptide containing residues 10−43 by NMR and circular dichroism (CD) experiments confirmed its unstructured conformation.[10] Therefore, the aggregation process in the WT protein is probably initiated by intermolecular interactions between the N-terminal region of adjacent monomers. For the phosphomimetic substitution at position 237, SEC or DLS analysis did not allow us to observe any difference between 3WA and 3WA/S237E, suggesting similar conformation for both proteins.

We then sought to assess whether the phosphomimetic mutation of serine 237 in the 3WA/S237E construct had any impact on protein solubility, as mentioned previously. To do this, protein samples of 3WA and 3WA/S237E in identical buffer conditions were concentrated by ultrafiltration until solubility limits were reached.[19,20] Interestingly, the relative solubility attained for the 3WA/S237E mutant (7.7 mg mL^{-1}) was double the observed value of 3WA (3.9 mg mL^{-1}); this value is also twice the concentration previously reported for the S239E mouse mutant.[17] These results suggest that the phosphomimetic mutation induces a structural change that increases solubility, most likely an electrostatic interaction with a neighboring residue since serine 237 is localized in the CAP that protects the putative active site.

Quadruple Mutant 3WA/S237E Shows Increased Thermal Stability Compared to the 3WA Mutant and Is Properly Folded. To evaluate the effect of mutations on CGI-58 stability, the thermal denaturation of CGI-58 WT, 3WA, and 3WA/S237E proteins was analyzed by a thermal displacement assay monitored by fluorescence (Figure 3). The apparent midpoint of thermal denaturation (T_m) was determined for the WT, 3WA, and 3WA/237E proteins in the optimized buffer; the observed values were 49.2 ± 0.5, 50.1 ± 0.4, and 51.7 ± 0.1 °C, respectively. The WT protein shows a sigmoid transition curve between 40 and 55 °C that looks extended and less pronounced when compared to the 3WA

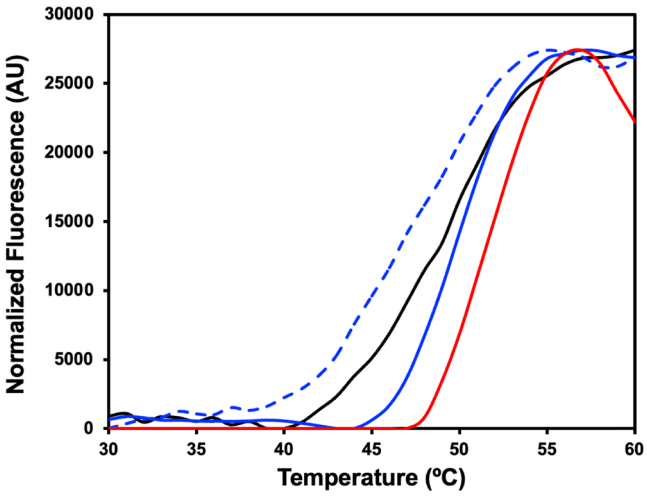

Figure 3. Thermal shift assays of CGI-58 WT, 3WA, and 3WA/S237E. Thermal denaturation curves of CGI-58 WT (black line), 3WA (blue line), and 3WA/S237E (red line) in the optimized buffer are shown [50 mM Tris−HCl, pH 8.0, 300 mM NaCl, 10% glycerol, 0.1% octyl glucoside, 6 mM dithiothreitol (DTT), and 15 mM β-mercaptoethanol (BME)]. The denaturation curve of 3WA (blue dashed line) in the nonoptimized buffer is also shown [15 mM Tris−HCl, pH 8.0, 85 mM NaCl, 2.85% glycerol, 0.03% octyl glucoside, 0.6 mM DTT, and 1.5 mM BME]. The estimated T_m values of 47.2 ± 0.5 (3WA nonoptimized buffer), 49.2 ± 0.5 (CGI-58 WT), 50.1 ± 0.4 (3WA), and 51.7 ± 0.1 °C (3WA/S237E) were calculated by adjusting data to the Boltzmann equation. The data shown correspond to the mean of three independent measurements.

https://doi.org/10.1021/acsomega.1c06872
ACS Omega 2022, 7, 12643−12653

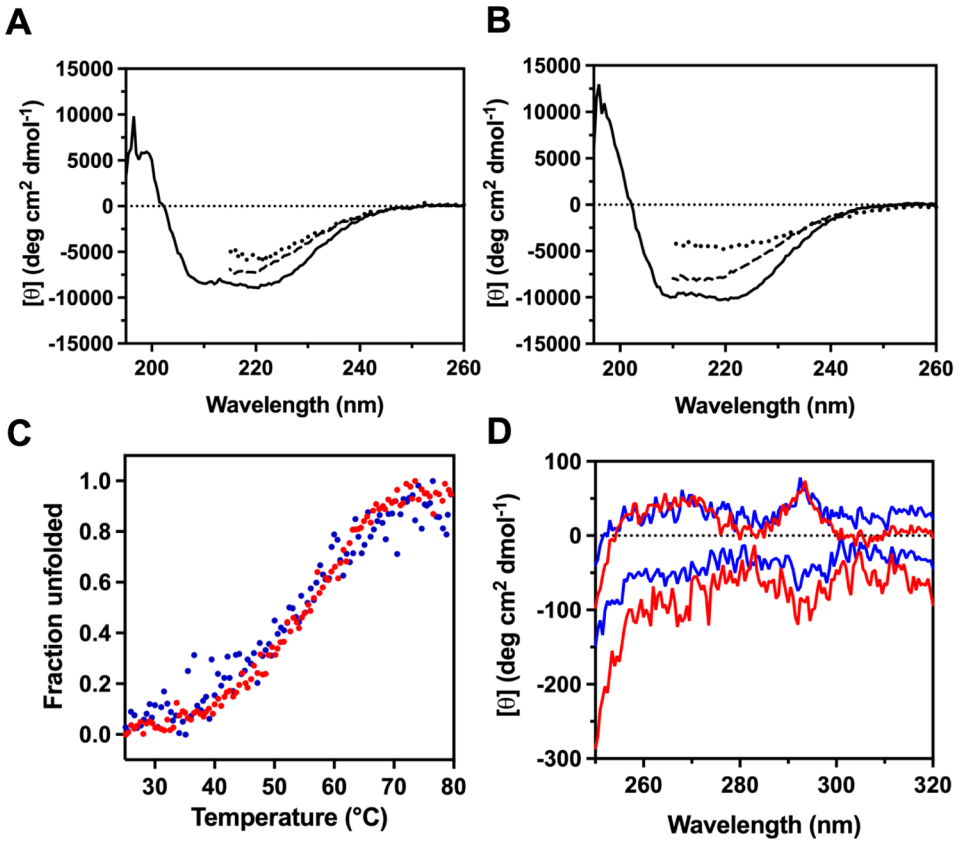

Figure 4. Analysis of 3WA and 3WA/S237E by CD spectroscopy. Far-UV CD spectra of (A) 3WA and (B) 3WA/S237E were recorded at 25 (black line), 65 (dashed line), and 80 °C (dotted line) at a protein concentration of 3.7 μM. To allow CD measurements, samples were prepared in 20 mM potassium phosphate, pH 8.0, 20 mM NaCl, 5% glycerol, and 0.1% octyl glucoside. (C) Thermal unfolding profiles of 3WA (blue line) and 3WA/S237E (red line) were monitored by CD spectroscopy at 222 nm. (D) Near-UV CD spectra of 3WA (blue line) and 3WA/S237E (red line) were recorded from 250 to 320 nm at 25 (upper lines) and 80 °C (bottom lines).

mutant. The WT and 3WA curves differ at the initial temperature of the transition but overlap at the upper region from 50 to 55 °C, indicating differences in the folded and unfolded states of the proteins, which may be explained by the presence of aggregates in the WT protein, as described previously.

In contrast to the profile observed for the WT protein, the thermal denaturation curve of 3WA and 3WA/S237E proteins is a pronounced sigmoid displaying a sharp transition when passing from the folded to the unfolded state, thus suggesting a homogeneous and compact folding of the proteins.[21] Interestingly, the quadruple 3WA/S237E mutant showed an increased thermal denaturation temperature, implying that the phosphomimetic mutation induces a structural change that improves thermal stability. The change in the thermostability of proteins in a positive, null, or negative way associated with a post-translational modification such as phosphorylation has been previously reported.[22] For example, a positive effect of ∼2 °C was reported for the phosphomimetic mutant (Cp183-EEE) of the arginine-rich C-terminal domain of Hepatitis B virus core protein,[23] and a similar positive effect of ∼2 °C was reported for the phosphomimetic mutation S17D in the N-terminal domain of MDM2.[24] It is worth mentioning that the estimated T_m value for the 3WA protein in the nonoptimized buffer was 47.2 °C, which is very similar to the values previously determined for the WT and S237E proteins by differential scanning fluorometry that were 47.4 and 46.2 °C, respectively.[25] Therefore, the use of the optimized buffer allowed us to observe the gain in thermal stability of ∼3.0 °C for 3WA compared to nonoptimized conditions, as well as to detect a difference of ∼1.0 °C between the WT and 3WA mutant and an improvement of ∼1.5 °C for 3WA/S237E compared to 3WA.

To gain more insight into the secondary structure content, thermal stability, and tertiary structure of 3WA and 3WA/S237E, we performed CD spectroscopy experiments.[26] Due to its high tendency to aggregate and poor solubility, CGI-58 WT was not subjected to further analysis. Figure 4A,B shows the CD spectra in the far-UV region of 3WA and 3WA/S237E at 25, 65, and 80 °C. At 25 °C, both proteins present the expected spectra commonly observed for an α/β protein with two negative peaks centered at approximately 210 (−8466.0 and −9970.6 deg·cm^2·dmol^{-1}, 3WA and 3WA/S237E, respectively) and 222 nm (−8610.8 and −10051.9 deg·cm^2·dmol^{-1}, 3WA and 3WA/S237E, respectively).

It is clear that although the far-UV CD spectra for both proteins are comparable, the recorded ellipticity values for 3WA were significantly lower than those for 3WA/S237E. This difference could be mainly attributed to the slight aggregation observed for 3WA when incubated in the buffer utilized for CD measurements. A spectrum analysis using the BeStSel web server[27] resulted in an estimated ∼24% content of α-helices, ∼29% of β-strands, ∼10% of β-turns, and ∼37% of coils for 3WA/S237E, which is close to the secondary structure prediction shown in Figure 1A. Secondary structure analysis of 3WA was not performed due to its slight tendency to

https://doi.org/10.1021/acsomega.1c06872
ACS Omega 2022, 7, 12643−12653

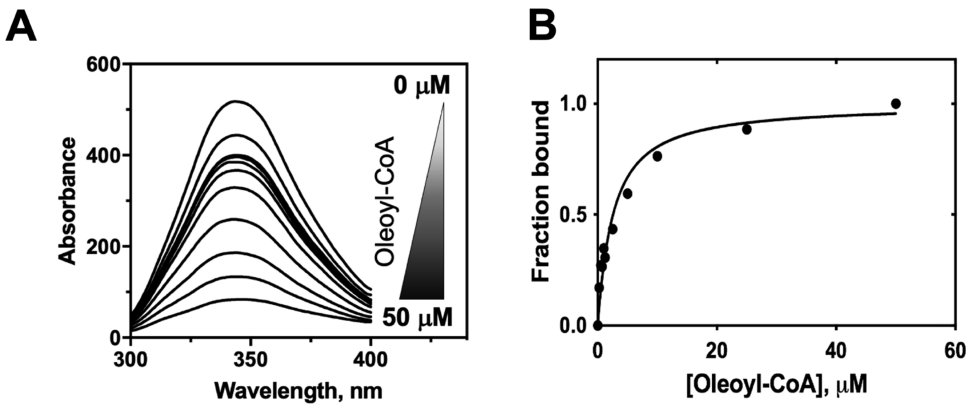

Figure 5. Intrinsic fluorescence affinity assays of 3WA/S237E in the presence of oleoyl-CoA. (A) Fluorescence spectra of 3WA/S237E with increasing concentrations of oleoyl-CoA. Fluorescence data were corrected for the inner filter effect. Assays were carried out with a 0.5 μM protein concentration at 25 °C; a representative experiment is shown. (B) Changes of fluorescence intensity at maximum fluorescence emission observed in (A) were plotted as a function of the concentration of oleoyl-CoA and analyzed for apparent K_d determination. The mean of three independent measurements is shown.

aggregate. Despite that, fold recognition for both proteins from CD data with the BeStSel server predicts the presence of the $\alpha\beta\alpha$ sandwich fold observed in the α/β hydrolase family.[28] At higher temperatures (65 and 80 °C), both proteins show a decrease in ellipticity, indicating that proteins undergo temperature-induced unfolding.

To further analyze the observed temperature-induced unfolding, thermal denaturation experiments were performed for both proteins by following the ellipticity change at 222 nm as a function of temperature (Figure 4C). In both cases, the transitions appear as single sigmoid curves. Data were fitted to a two-state model of protein unfolding, which allowed us to estimate the midpoint of thermal denaturation and apparent enthalpy change (ΔH_D). The thermal stability of 3WA/S237E (T_m of 57.5 ± 1.0 °C) was 3.1 °C higher than that of 3WA (T_m of 54.4 ± 1.1 °C). Similarly, the unfolding ΔH_D of 3WA/S237E (158.8 ± 2.8 kJ mol^{-1}) was higher than that of 3WA (150.9 ± 2.0 kJ mol^{-1}). The increased thermal stability observed for 3WA/S237E is consistent with the thermal shift results described above and suggests that the phosphomimetic substitution induces a structural change, most likely favorable intramolecular interactions, that stabilize the 3WA/S237E structure.[29] Furthermore, the apparent enthalpy change associated with the unfolding reactions indicates a more cooperative reaction for 3WA/S237E, which could be attributed to a, although modest, non-negligible increment in the number or robustness of tertiary contacts.

To examine the tertiary structure of both proteins, the CD spectra in the near-UV region (250 to 320 nm) were analyzed. Near-UV CD spectra provide evidence of the tertiary structure since, when located in chiral environments, aromatic amino acid side chains have a characteristic CD profile that provides a fingerprint of a particular protein.[30]

Although relatively low protein concentration (0.15 mg mL^{-1}) was used for CD experiments, since low protein stability was observed in the reaction buffer (Figure 4D), the expected peak close to 290 nm for tryptophan residues was observed together with a broad positive region between 260 and 280 nm, which could correspond to the signal of tyrosine and phenylalanine residues. Both spectra overlap from 250 to 300 nm, suggesting that the tertiary structure of 3WA/S237E is similar to that of the 3WA mutant. In both cases, increasing the temperature resulted in the loss of signal at 290 nm and from 260 to 280 nm, meaning that the environment around aromatic residues has changed as a consequence of thermal denaturation.

Taken together, the far-UV CD data indicate that 3WA and 3WA/S237E maintain the secondary structure characteristic of the α/β hydrolase family. Thermal denaturation experiments confirmed the more stable conformation of 3WA/S237E, and the apparent ΔH_D suggests that 3WA/S237E is stabilized by the enhancement of intramolecular interactions due to the presence of the phosphomimetic glutamic acid at position 237. Moreover, a similar tertiary structure can be inferred between both proteins from the near-UV CD results.

Quadruple Mutant 3WA/S237E Has a Functional Binding Site for Oleoyl-CoA. Previous studies have found that oleoyl-CoA is an endogenous ligand of human CGI-58 that shares a common binding site with synthetic compounds.[13] Binding of oleoyl-CoA to mouse CGI-58 has also been reported.[31] Considering this information, we were interested in knowing whether the 3WA/S237E protein has a functional binding site for oleoyl-CoA. To determine the binding affinity toward oleoyl-CoA, we performed tryptophan fluorescence spectroscopy experiments. This approach has been frequently used to study ligand binding to proteins,[32] and the analysis of fluorescence quenching data has been recently reviewed.[33] Figure 5A shows a representative example of the fluorescence emission spectra of 3WA/S237E in the presence of increasing concentrations of oleoyl-CoA. The observed fluorescence data for oleoyl-CoA were corrected for the inner filter effect, as samples of the ligand showed significant absorbance at an excitation wavelength of 280 nm, with a value of 0.2 at a higher concentration of 50 μM. The addition of increasing concentrations of oleoyl-CoA to 3WA/S237E resulted in a progressive reduction of fluorescence intensity, probably due to the induced structural changes around aromatic residues, suggesting its interaction with the protein.

At the highest concentration of oleoyl-CoA, we observed 65% fluorescence quenching. Changes in the fluorescence intensity were plotted versus ligand concentration and analyzed to determine the ligand's apparent dissociation constant (K_d). Oleoyl-CoA showed an apparent K_d of 2.3 ± 0.3 μM (Figure 5B). This result suggests that the 3WA/S237E mutant has a functional and probably intact ligand-binding site since our results are similar to the values reported for the

https://doi.org/10.1021/acsomega.1c06872
ACS Omega 2022, 7, 12643−12653

mouse CGI-58 protein, which shows an apparent K_d of 1.1 μM for oleoyl-CoA.[31] Compared to the mouse orthologue, the 3WA/S237E protein showed two times lower affinity for oleoyl-CoA.

Insights into the Structural Role of Residue S237. To gain more insight into how the phosphomimetic mutation of residue S237 increases the stability and solubility of 3WA/S237E, we generate bioinformatic three-dimensional (3D) models (Supporting Information) to analyze possible intramolecular contacts as the crystallographic structure of CGI-58 has not yet been determined. Figure 6 shows the 3D models

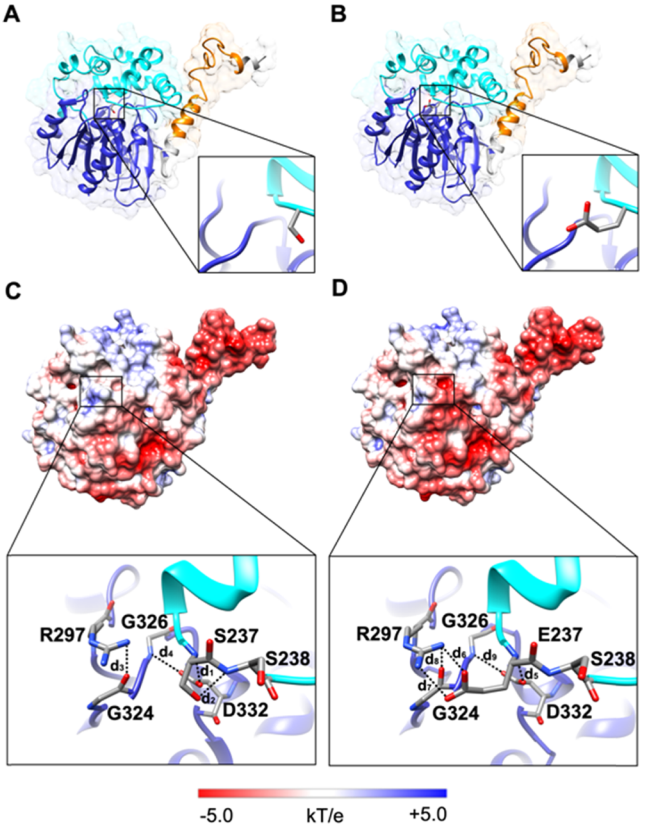

Figure 6. Electrostatic and molecular contact analysis of serine 237 (CGI-58 WT) and its phosphomimetic substitution with glutamic acid (S237E). Ribbon representation of (A) WT and (B) S237E, the LD-binding motif is orange (residues 8−41), the α/β hydrolase core is blue (residues 52−349), and the cap of the active site is cyan (residues 178−276). The inset of (A) shows serine 237 (CGI-58 WT), while the inset of (B) shows phosphomimetic glutamic acid (S237E). The surface electrostatic potentials of WT and S237E are shown in (C) and (D), respectively. Positively charged regions are blue, and negatively charged regions are red. (C) Close-up view of S237 and adjacent residues (R297, G324, G326, and D332). (D) Close-up view of phosphomimetic glutamic acid (S237E) and the aforementioned adjacent residues. Dashed lines indicate intramolecular interactions between pairs of atoms; corresponding distances are listed in Table 1.

generated for CGI-58; high similarity is observed in the topology of α-helices and β-strands connected by loops with the α/β hydrolase family. The α/β hydrolase core, the active site cap, and the LD attachment sequence are depicted as described in Figure 1A. Figure 6A shows the loop of residues 236−242, where S237 is located, approximately in the middle of the active site cap. The model shows that the side chain of S237 makes a hydrogen bond with the main chain N of S238 (Oγ − N 2.87 Å), while the main chain N of S237 forms a hydrogen bond with the side chain of D332 (N − Oδ_1 2.77 Å) (Figure 6C inset). Neighboring residues of S237 included R297, which makes a hydrogen bond with the carbonyl O of G324 (Nη_1 − O 2.94 Å). Table 1 shows the distances of the

Table 1. Molecular Distances between Serine or Glutamic Acid Residue at Position 237 and Nearby Residues

protein	$d(a_1, a_2)$[a]	a_1	a_2	distance, Å
WT	1	S237 (N)	Asp332 (Oδ_1)	2.77
	2	S237 (Oγ)	Ser238 (N)	2.87
	3	Arg297 (Nη1)	Gly324 (O)	2.94
	4	Gly326 (N)	Asp332 (Oδ_2)	2.82
S237E	5	E237 (N)	Asp332 (Oδ_1)	2.80
	6	E237 (Oε_1)	Arg297(Nη_1)	2.71
	7	E237 (Oε_2)	Arg297(Nη_2)	2.77
	8	Arg297 (Nη1)	Gly324 (O)	2.93
	9	Gly326 (N)	Asp332 (Oδ_2)	2.83

[a]Measured distances for specific pairs of atoms $d(a_1, a_2)$ are shown in Å. Shown in Figure 6.

intramolecular interactions of S237 and the neighboring residues. The interactions described above differ from those reported for the mouse protein. In the computational model for mouse CGI-58, the R299 (R297 in human CGI-58) interacts via a salt bridge with the side chain of D334 (D332 in human CGI-58),[7] indicating some differences to the human model. However, in both cases, arginine interacts with residues of the α/β hydrolase core.

The replacement of S237 with glutamic acid (E237) causes changes to the intramolecular interactions, as shown in Figure 6D and Table 1. The side chain of E237 is directed toward the loop where R297 is located. This change of orientation causes the negative charges of Oε_1 and Oε_2 of E237 to form interactions with the positive charges of Nη_1 and Nη_2 of R297, respectively. According to the distances between atoms (Oε_1 − Nη_1, 2.71 Å; and Oε_2 − Nη_2, 2.77 Å), these form a salt bridge, suggesting the stabilization of the active site cap and, in particular, R297, which has been reported as essential in the activation of ATGL.[7] Other residues that were identified at a close distance (5 Å cutoff) that could participate in an intramolecular interaction with E237 included A325 and G324 (main chain *N* at 4. 3 and 4.4 Å, respectively) and the side chain of Q333 (at 4.8 Å). Interestingly, R297, A325, G324, and Q333 are located in the α/β hydrolase core of the protein.

The above analysis suggests that the side chain of S237 in the WT protein plays a local role by interacting through a hydrogen bond with the main chain N of S238; both residues are located at the active site cap. According to our interpretation of possible contacts of E237, the phosphomimetic substitution could have a global structural effect since this residue could interact with a residue of the α/β hydrolase core. This suggests that the phosphomimetic substitution works as an anchor that fixes the cap on the α/β hydrolase core, which favors a more stable conformation of CGI-58.

In summary, our results revealed that N-terminal tryptophan residues (W19, W23, and W27) function as a nucleation site that promotes aggregation of CGI-58. This suggests that in a cellular context, interaction with PLIN1 in the LD or with ATGL stabilizes CGI-58 preventing its aggregation. Solubility and thermal stability results demonstrate that the phosphomi-

https://doi.org/10.1021/acsomega.1c06872
ACS Omega 2022, 7, 12643−12653

metic mutation of S237 improves the solubility and stability of CGI-58. The ligand binding analyses where we observed affinities similar to those of the mouse ortholog, together with the CD spectroscopy results in the far- and near-UV regions, suggest that the quadruple mutant (3WA/S237E) is functional and maintains the native conformation. Furthermore, the analysis of bioinformatic models suggests an intramolecular interaction between the side chain of glutamic acid 237, located at the CAP that protects the potential catalytic site, with a residue in the α/β hydrolase core, resulting in a more compact and stable conformation of CGI-58.

MATERIALS AND METHODS

Bioinformatics Analysis of CGI-58. Human (Q8WTS1.1) and mouse (Q9DBL9.1) CGI-58 protein sequences were downloaded from the NCBI website. A sequence alignment was carried out using the T-Coffe web server.[34] Protein secondary structure prediction was performed using Jpred4 (https://www.compbio.dundee.ac.uk/jpred/)[35] and PredictProtein (https://predictprotein.org/home)[36] web servers. Aggregation propensity analysis of protein sequences was performed using AGGRESCAN[14] with default parameters.

Cloning and Mutagenesis. The coding DNA sequence for human CGI-58 (NP_001342115) was optimized for bacterial expression and acquired from GeneOracle in the pGOV4 plasmid. The gene was amplified by PCR with forward primer 5′-GTAATTCCATATGGCAGCGGAAGAGGAAGAGG and reverse primer 5′-CGCGGATCCAAGCTTTCAATCGACAG. PCR amplification was performed with *Platinum Taq* polymerase (Invitrogen). The amplified DNA fragment was digested using *Nde*I and *Hind*III restriction enzymes and ligated to the *Nde*I and *Hind*III sites of a modified pET28a vector in which the thrombin site was substituted by the human rhinovirus 3C protease site. Triple mutant W19A/W23A/W27A (3WA) and quadruple mutant 3WA/S237E were generated by PCR using the primers listed in Table S1. All constructs were verified by sequencing.

Recombinant Protein Expression and Purification. The plasmid encoding full-length CGI-58 WT sequence or mutant constructs were transformed into *Escherichia coli* BL21-CodonPlus (DE3)-RIPL competent cells according to the manufacturer's instructions and were cultured for 4 h at 37 °C in Luria broth (LB) containing kanamycin (50 μg mL^{-1}). When the bacterial culture reached an OD_{600} of 0.6−0.8, protein expression was induced by adding IPTG to a final concentration of 0.5 mM and further cultured for 24 h at 18 °C and shaking at 200 rpm. The cells were collected by centrifugation at 12,000 rpm for 15 min at 4 °C, and the pellet was stored at −20 °C until use or immediately sonicated at 4 °C in buffer A [50 mM Tris−HCl, pH 8.0, 300 mM NaCl, 10% (v/v) glycerol, 1% (w/v) octyl glucoside, 6 mM DTT, 15 mM BME and 10 mM imidazole]. The cell lysate was clarified by centrifugation, and the supernatant was loaded onto a Ni-NTA column (Qiagen) equilibrated with buffer A. The column was washed with three column volumes (CVs) of buffer B [50 mM Tris−HCl, pH 8.0, 300 mM NaCl, 10% (v/v) glycerol, 0.1% (w/v) octyl glucoside, 6 mM DTT, 15 mM BME, and 10 mM imidazole]. Elution of the recombinant protein was carried out in one step with three CVs of buffer B supplemented with 500 mM imidazole. The fractions containing the recombinant protein were pooled and incubated overnight at 4 °C using 5 units mL^{-1} HRV 3C protease to remove 6XHis-tag. Full cleavage of 6XHis-tag was monitored by Western blot analysis. The tag-free protein was buffer exchanged on a PD-10 column into buffer C [50 mM Tris−HCl, pH 8.0, 100 mM NaCl, 10% (v/v) glycerol, 0.1% (w/v) octyl glucoside, 6 mM DTT, and 15 mM BME] and loaded into a HiTrap-Q HP column (GE Healthcare). The recombinant protein was eluted with a linear gradient from 100 to 500 mM of NaCl in buffer C (15 CV). The fractions containing the eluted protein were pooled and concentrated using an ultrafiltration device (Sartorius Vivaspin Turbo 15, 10 kDa) and further fractionated through a Superdex-200 10/300 GL column (GE Healthcare) in the optimized buffer [50 mM Tris−HCl, pH 8.0, 300 mM NaCl, 10% (v/v) glycerol, 0.1% (w/v) octyl glucoside, 6 mM DTT, and 15 mM BME]. The standard protein yield obtained at the end of purification was 0.36, 1.6, and 4.8 mg L^{-1} for the WT, 3WA, and 3WA/S237E, respectively. The optimal concentrations of glycerol, octyl glucoside, DTT, and BME used in the optimized buffer were determined for the 3WA mutant by the thermal stability assay and then used for WT, 3WA, and 3WA/S237E protein purification (supplementary data, Table S2). The Superdex-200 10/300 GL column was calibrated with protein markers: thyroglobulin (670 kDa), γ-globulin (158 kDa), ovalbumin (44 kDa), myoglobin (17 kDa), and vitamin B12 (1.3 kDa). Qualitative evaluation of protein expression and purification procedures was monitored by SDS-PAGE. The protein concentration was determined by the Bradford assay using BSA as the protein standard.

Protein Solubility Measurements. Relative solubility limits of 3WA and 3WA/S237E proteins were measured by ultrafiltration. For this, protein samples were prepared in the optimized buffer and concentrated until the protein concentration in the retained solution remained constant; the retained solution was replenished as needed. A 10 kDa cutoff Sartorius Vivaspin Turbo 15 concentrator was used at 3000*g* at 4 °C. Samples were mixed regularly by pipetting to prevent membrane blockage. The protein concentration was measured by taking 10 μL aliquots at several intervals. When the maximum concentration in the retained solution was reached, samples were transferred to a 1.5 mL centrifuge tube followed by incubation overnight at 4 °C. After that, samples were centrifugated for 15 min at 15,000 rpm at 4 °C to discard any precipitated protein before measuring the protein concentration.

Dynamic Light Scattering (DLS). DLS assays were carried out using an APS2000 system (Malvern Instruments). Hydrodynamic radius (R_h) measurements were performed at a protein concentration of 0.4 mg mL^{-1} in the optimized buffer [50 mM Tris−HCl, pH 8.0, 300 mM NaCl, 10% (v/v) glycerol, 0.1% (w/v) octyl glucoside, 6 mM DTT, and 15 mM BME]. The instrument was programmed to perform 15 scans of 40 s each at 25 °C; samples were incubated for 5 min at 25 °C for equilibration before measurements. The molecular weight was estimated from the R_h using Malvern Zetasizer software version 7.13.

Thermal Stability Assay. Protein thermal stability determination was carried out on 96-well plates using a 7500 Fast Real-Time PCR system (Applied Biosystems). Samples containing the condition to be evaluated, 5X SYPRO ORANGE (Invitrogen) and 0.05 mg mL^{-1} protein, were prepared at a final volume of 40 μL. Preliminary thermal denaturation experiments were performed in a temperature range from 25 to 95 °C with increments of 1 °C and 30 s incubation at each step. Once the temperature range for the

https://doi.org/10.1021/acsomega.1c06872
ACS Omega 2022, 7, 12643−12653

thermal transition curve was identified, the temperature range was delimited as indicated in the corresponding figure for triplicate measurements. Protein unfolding was followed by monitoring fluorescence, an excitation wavelength of 455−485 was used, and emission was recorded between 567 and 596 nm. The fluorescence intensity of protein samples was corrected by subtracting the fluorescence intensity of control samples without proteins. The melting curve was obtained by plotting the corrected fluorescence intensities as a function of the temperature. The data were fitted to the Boltzmann equation for T_m determination as recommended by Lee et al.[37]

Fluorescence Quenching Assays. Intrinsic fluorescence data were acquired on an LS 55 spectrofluorometer (Perkin Elmer). The emission-fluorescence spectra were monitored from 300 to 400 nm at an excitation wavelength of 280 nm. Samples of 0.5 μM protein were prepared in the optimized buffer [50 mM Tris−HCl, pH 8.0, 300 mM NaCl, 10% (v/v) glycerol, 0.1% (w/v) octyl glucoside, 6 mM DTT, and 15 mM BME]. Data were obtained at 25 °C with or without increasing concentrations of oleoyl-CoA until quenching reached a plateau. Fluorescence spectra of the buffer were measured and subtracted from spectra of the protein samples. The presence of any inner filter effect was evaluated by recording the absorption of ligands at the excitation and emission wavelengths at the same concentrations used for fluorescence experiments. If detected, each fluorescence spectrum was corrected using eq 1, where F_{cor} and F_{obs} are the corrected and observed fluorescence intensities, respectively, and A_{ex} and A_{em} represent the differences in the absorbance values of the sample upon the addition of the ligand at the excitation (280 nm) and emission (300−400 nm) wavelengths, respectively.[33]

$$F_{cor} = F_{obs} \times 10^{(A_{ex}+A_{em})/2} \quad (1)$$

To estimate the apparent dissociation constant (K_d), the changes in the fluorescence intensity at the maximum emission wavelength were plotted as a function of the ligand concentration and analyzed by a nonlinear curve fitting to the quadratic equation (eq 2) using GraphPad PRISM 8.

$$\text{fraction bound} = \frac{[P]_t + [L]_t + K_d - \sqrt{([P]_t + [L]_t + K_d)^2 - 4[P]_t[L]_t}}{2[P]_t} \quad (2)$$

where $[P]_t$ is the total protein concentration and $[L]_t$ is the total ligand concentration. This approach can be applied when $[P]_t \ll K_d$ or when $[P]_t$ is similar to or in modest excess over the K_d (~10-fold excess).[38] All reported values are the means of three independent experiments.

Circular Dichroism Analysis. Spectra were acquired in a J-815 CD spectropolarimeter (Jasco Inc., Easton, MD) equipped with a Peltier thermal device (PFD-425S) for temperature control. Due to the high absorbance of the optimized buffer at low wavelengths in the UV region, samples were prepared at a protein concentration of 3.7 μM in the following buffer [20 mM potassium phosphate, pH 8.0, 20 mM NaCl, 5% (v/v) glycerol, 0.1% (w/v) octyl glucoside]. Far-UV CD data were recorded from 192.5 to 250 nm using a 0.1 cm path length quartz cuvette at 25, 65, and 80 °C. Near-UV CD spectra were recorded from 250 to 320 nm using a 1.0 cm path length cuvette at 25 and 80 °C. Ellipticity is reported as mean ellipticity per residue [θ].[26] The secondary structure content was estimated from CD data using the BestSel web server (http://bestsel.elte.hu/).[27]

Thermal denaturation experiments were performed by increasing the temperature of samples from 25 to 80 °C at a constant heating rate of 2 °C min^{-1} while recording changes in ellipticity at 222 nm. Protein concentrations and buffer conditions were the same as described above. Experimental CD data were analyzed assuming a two-state transition model between the native (N) and the unfolded (D) monomer with no intermediate state.[39]

$$N \leftrightharpoons D \quad (3)$$

The equilibrium constant of the reaction is defined as

$$K_D = \frac{[D]}{[N]} \quad (4)$$

The fraction of unfolded protein, according to eq 5,

$$f_D = \frac{[D]}{P_t} \quad (5)$$

where P_t is the total concentration of the protein in monomer units.

The calculation of the enthalpy change (ΔH_D) associated with thermal denaturation was carried out using the classical thermodynamic relationship[40]

$$\Delta H_U(T) = -R[\partial \ln K_U/\partial(1/T)] = RT^2(\partial \ln K_D/\partial T) \quad (6)$$

$$\Delta S_U(T_m) = \Delta H_U(T_m)/T_m \quad (7)$$

where T_m is the midpoint of thermal denaturation. van't Hoff plots ($\ln K_U$ vs $1/T$) of thermal denaturation are approximately linear through the T_m region, allowing an estimation of the enthalpy and entropy of unfolding at T_m.

Three-Dimensional Structural Modeling. The three-dimensional (3D) model of full-length CGI-58 was generated using the online I-TASSER web server.[41] The 3D model generated by I-TASSER was energy-minimized by a 100-step protocol in UCSF Chimera.[42] The WT minimized structure was used as a template to generate the mutant S237E. For this, the side chain of S237 was substituted by glutamic acid with COOT software.[43] The model was subjected to another round of energy minimization to improve side-chain rotamers, hydrogen bonding, and remove atom clashes. Electrostatic potentials were calculated using the PDB2PQR web server and the Adaptative Poisson-Boltzmann Solver APBS;[44] the implicit solvent calculation was performed with the PARSE force field, while protonation states were assigned with PROPKA. Molecular visualization and depiction were performed with UCSF CHIMERA.[42]

■ ASSOCIATED CONTENT

Supporting Information

The Supporting Information is available free of charge at https://pubs.acs.org/doi/10.1021/acsomega.1c06872.

Oligonucleotides used for cloning and mutagenesis experiments (Table S1) and apparent melting temperatures (T_m) for the 3WA mutant in the presence of several additives (Table S2) (PDF)

CGI-58 WT and S237E bioinformatic 3D models (ZIP)

https://doi.org/10.1021/acsomega.1c06872
ACS Omega 2022, 7, 12643−12653

AUTHOR INFORMATION

Corresponding Authors

Samuel Lara-González − *IPICYT, División de Biología Molecular, Instituto Potosino de Investigación Científica y Tecnológica A.C., San Luis Potosí, San Luis Potosí 78216, México;* orcid.org/0000-0002-3313-0165; Email: samuel.lara@ipicyt.edu.mx

Gabriela M. Montero-Morán − *Universidad Autónoma de San Luis Potosí, Facultad de Ciencias Químicas, San Luis Potosí, San Luis Potosí 78210, México*; Email: gabriela.montero@uaslp.mx

Authors

Miriam Livier Llamas-García − *IPICYT, División de Biología Molecular, Instituto Potosino de Investigación Científica y Tecnológica A.C., San Luis Potosí, San Luis Potosí 78216, México*

Edgar D. Páez-Pérez − *IPICYT, División de Biología Molecular, Instituto Potosino de Investigación Científica y Tecnológica A.C., San Luis Potosí, San Luis Potosí 78216, México;* orcid.org/0000-0003-2906-2953

Claudia G. Benitez-Cardoza − *Laboratorio de Investigación Bioquímica, Escuela Nacional de Medicina y Homeopatía, Instituto Politécnico Nacional, Ciudad de México 07320, México*

Complete contact information is available at: https://pubs.acs.org/10.1021/acsomega.1c06872

Notes

The authors declare no competing financial interest.

ACKNOWLEDGMENTS

This work was supported by CONACyT [grant number CB-168710 to S.L.-G. and INFRA-204373]. M.L.L.-G. thanks CONACyT for the fellowship [#395867].

REFERENCES

(1) Lai, C. H.; Chou, C. Y.; Ch'ang, L. Y.; Liu, C. S.; Lin, W. C. Identification of Novel Human Genes Evolutionarily Conserved in *Caenorhabditis elegans* by Comparative Proteomics. *Genome Res.* **2000**, *10*, 703−713.

(2) Lefèvre, C.; Jobard, F.; Caux, F.; Bouadjar, B.; Karaduman, A.; Heilig, R.; Lakhdar, H.; Wollenberg, A.; Verret, J. L.; Weissenbach, J.; Özgüc, M.; Lathrop, M.; Prud'lhomme, J. F.; Fischer, J. Mutations in CGI-58, the Gene Encoding a New Protein of the Esterase/Lipase/Thioesterase Subfamily, in Chanarin-Dorfman Syndrome. *Am. J. Hum. Genet.* **2001**, *69*, 1002−1012.

(3) Kulminskaya, N.; Oberer, M. Protein-Protein Interactions Regulate the Activity of Adipose Triglyceride Lipase in Intracellular Lipolysis. *Biochimie* **2020**, *169*, 62−68.

(4) Yu, L.; Li, Y.; Grisé, A.; Wang, H. CGI-58: Versatile Regulator of Intracellular Lipid Droplet Homeostasis. *Adv. Exp. Med. Biol.* **2020**, *1276*, 197−222.

(5) Zierler, K. A.; Zechner, R.; Haemmerle, G. Comparative Gene Identification-58/α/β Hydrolase Domain 5: More than Just an Adipose Triglyceride Lipase Activator? *Curr. Opin. Lipidol.* **2014**, *25*, 102−109.

(6) Gruber, A.; Cornaciu, I.; Lass, A.; Schweiger, M.; Poeschl, M.; Eder, C.; Kumari, M.; Schoiswohl, G.; Wolinski, H.; Kohlwein, S. D.; Zechner, R.; Zimmermann, R.; Oberer, M. The N-Terminal Region of Comparative Gene Identification-58 (CGI-58) Is Important for Lipid Droplet Binding and Activation of Adipose Triglyceride Lipase. *J. Biol. Chem.* **2010**, *285*, 12289−12298.

(7) Sanders, M. A.; Zhang, H.; Mladenovic, L.; Tseng, Y. Y.; Granneman, J. G. Molecular Basis of ABHD5 Lipolysis Activation. *Sci. Rep.* **2017**, *7*, No. 42589.

(8) Eichmann, T. O.; Kumari, M.; Haas, J. T.; Farese, R. V.; Zimmermann, R.; Lass, A.; Zechner, R. Studies on the Substrate and Stereo/Regioselectivity of Adipose Triglyceride Lipase, Hormone-Sensitive Lipase, and Diacylglycerol-O- Acyltransferases. *J. Biol. Chem.* **2012**, *287*, 41446−41457.

(9) Subramanian, V.; Rotlienberg, A.; Gomez, C.; Cohen, A. W.; Garcia, A.; Bhattacharyya, S.; Shapiro, L.; Dolios, G.; Wang, R.; Lisanti, M. P.; Brasaemle, D. L. Perilipin A Mediates the Reversible Binding of CGI-58 to Lipid Droplets in 3T3-L1 Adipocytes. *J. Biol. Chem.* **2004**, *279*, 42062−42071.

(10) Boeszoermenyi, A.; Nagy, H. M.; Arthanari, H.; Pillip, C. J.; Lindermuth, H.; Luna, R. E.; Wagner, G.; Zechner, R.; Zangger, K.; Oberer, M. Structure of a CGI-58 Motif Provides the Molecular Basis of Lipid Droplet Anchoring. *J. Biol. Chem.* **2015**, *290*, 26361−26372.

(11) Granneman, J. G.; Moore, H. P. H.; Krishnamoorthy, R.; Rathod, M. Perilipin Controls Lipolysis by Regulating the Interactions of AB-Hydrolase Containing 5 (Abhd5) and Adipose Triglyceride Lipase (Atgl). *J. Biol. Chem.* **2009**, *284*, 34538−34544.

(12) Sahu-Osen, A.; Montero-Moran, G.; Schittmayer, M.; Fritz, K.; Dinh, A.; Chang, Y. F.; McMahon, D.; Boeszoermenyi, A.; Cornaciu, I.; Russell, D.; Oberer, M.; Carman, G. M.; Birner-Gruenberger, R.; Brasaemle, D. L. CGI-58/ABHD5 Is Phosphorylated on Ser239 by Protein Kinase A: Control of Subcellular Localization. *J. Lipid Res.* **2015**, *56*, 109−121.

(13) Sanders, M. A.; Madoux, F.; Mladenovic, L.; Zhang, H.; Ye, X.; Angrish, M.; Mottillo, E. P.; Caruso, J. A.; Halvorsen, G.; Roush, W. R.; Chase, P.; Hodder, P.; Granneman, J. G. Endogenous and Synthetic ABHD5 Ligands Regulate ABHD5-Perilipin Interactions and Lipolysis in Fat and Muscle. *Cell Metab.* **2015**, *22*, 851−860.

(14) Conchillo-Solé, O.; de Groot, N. S.; Avilés, F. X.; Vendrell, J.; Daura, X.; Ventura, S. AGGRESCAN: A Server for the Prediction and Evaluation of "Hot Spots" of Aggregation in Polypeptides. *BMC Bioinf.* **2007**, *8*, No. 65.

(15) De Groot, N. S.; Pallarés, I.; Avilés, F. X.; Vendrell, J.; Ventura, S. Prediction of "Hot Spots" of Aggregation in Disease-Linked Polypeptides. *BMC Struct. Biol.* **2005**, *5*, No. 18.

(16) Graña-Montes, R.; de Oliveira, R. S. A.; Ventura, S. Protein Aggregation Profile of the Human Kinome. *Front. Physiol.* **2012**, *3*, No. 438.

(17) Hofer, P.; Boeszoermenyi, A.; Jaeger, D.; Feiler, U.; Arthanari, H.; Mayer, N.; Zehender, F.; Rechberger, G.; Oberer, M.; Zimmermann, R.; Lass, A.; Haemmerle, G.; Breinbauer, R.; Zechner, R.; Preiss-Landl, K. Fatty Acid-Binding Proteins Interact with Comparative Gene Identification-58 Linking Lipolysis with Lipid Ligand Shuttling. *J. Biol. Chem.* **2015**, *290*, 18438−18453.

(18) Phillips, K.; de la Peña, A. H. The Combined Use of the Thermofluor Assay and ThermoQ Analytical Software for the Determination of Protein Stability and Buffer Optimization as an Aid in Protein Crystallization. *Curr. Protoc. Mol. Biol.* **2011**, 1−15.

(19) Evans, P.; Wyatt, K.; Wistow, G. J.; Bateman, O. A.; Wallace, B. A.; Slingsby, C. The P23T Cataract Mutation Causes Loss of Solubility of Folded ΓD-Crystallin. *J. Mol. Biol.* **2004**, *343*, 435−444.

(20) Golovanov, A. P.; Hautbergue, G. M.; Wilson, S. A.; Lian, L. Y. A Simple Method for Improving Protein Solubility and Long-Term Stability. *J. Am. Chem. Soc.* **2004**, *126*, 8933−8939.

(21) Reinhard, L.; Geerlof, A.; Mueller-dieckmann, J.; Weiss, M. S.; Vej, G. W.; Cedex, F.-G. Optimization of Protein Buffer Cocktails Using Thermofluor. *Acta Crystallogr., Sect. F: Struct. Biol. Commun.* **2013**, *F69*, 209−214.

(22) Huang, J. X.; Lee, G.; Cavanaugh, K. E.; Chang, J. W.; Gardel, M. L.; Moellering, R. E. High Throughput Discovery of Functional Protein Modifications by Hotspot Thermal Profiling. *Nat. Methods* **2019**, *16*, 894−901.

(23) Selzer, L.; Kant, R.; Wang, J. C. Y.; Bothner, B.; Zlotnick, A. Hepatitis B Virus Core Protein Phosphorylation Sites Affect Capsid

https://doi.org/10.1021/acsomega.1c06872
ACS Omega 2022, 7, 12643−12653

Stability and Transient Exposure of the C-Terminal Domain. *J. Biol. Chem.* **2015**, *290*, 28584−28593.
(24) Worrall, E. G.; Worrall, L.; Blackburn, E.; Walkinshaw, M.; Hupp, T. R. The Effects of Phosphomimetic Lid Mutation on the Thermostability of the N-Terminal Domain of MDM2. *J. Mol. Biol.* **2010**, *398*, 414−428.
(25) Jebessa, Z. H.; Shanmukha, K. D.; Dewenter, M.; Lehmann, L. H.; Xu, C.; Schreiter, F.; Siede, D.; Gong, X. M.; Worst, B. C.; Federico, G.; Sauer, S. W.; Fischer, T.; Wechselberger, L.; Müller, O. J.; Sossalla, S.; Dieterich, C.; Most, P.; Gröne, H. J.; Moro, C.; Oberer, M.; Haemmerle, G.; Katus, H. A.; Tyedmers, J.; Backs, J. The Lipid-Droplet-Associated Protein ABHD5 Protects the Heart through Proteolysis of HDAC4. *Nat. Metab.* **2019**, *1*, 1157−1167.
(26) Greenfield, N. J. Using Circular Dichroism Spectra to Estimate Protein Secondary Structure. *Nat. Protoc.* **2007**, *1*, 2876−2890.
(27) Micsonai, A.; Wien, F.; Bulyáki, É.; Kun, J.; Lee, Y.-H.; Goto, Y.; Réfregiers, M.; Kardos, J.; Matthieu, R. BeStSel: A Web Server for Accurate Protein Secondary Structure Prediction and Fold Recognition from the Circular Dichroism Spectra. *Nucleic Acids Res.* **2018**, *46*, 315−322.
(28) Lord, C. C.; Thomas, G.; Brown, J. M. Mammalian Alpha Beta Hydrolase Domain (ABHD) Proteins: Lipid Metabolizing Enzymes at the Interface of Cell Signaling and Energy Metabolism. *Biochim. Biophys. Acta, Mol. Cell Biol. Lipids* **2013**, *1831*, 792−802.
(29) Yamniuk, A. P.; Ishida, H.; Lippert, D.; Vogel, H. J. Thermodynamic Effects of Noncoded and Coded Methionine Substitutions in Calmodulin. *Biophys. J.* **2009**, *96*, 1495−1507.
(30) Kelly, S. M.; Jess, T. J.; Price, N. C. How to Study Proteins by Circular Dichroism. *Biochim. Biophys. Acta, Proteins Proteomics* **2005**, *1751*, 119−139.
(31) Montero-Moran, G.; Caviglia, J. M.; McMahon, D.; Rothenberg, A.; Subramanian, V.; Xu, Z.; Lara-Gonzalez, S.; Storch, J.; Carman, G. M.; Brasaemle, D. L. CGI-58/ABHD5 Is a Coenzyme A-Dependent Lysophosphatidic Acid Acyltransferase. *J. Lipid Res.* **2010**, *51*, 709−719.
(32) Sindrewicz, P.; Li, X.; Yates, E. A.; Turnbull, J. E.; Lian, L. Y.; Yu, L. G. Intrinsic Tryptophan Fluorescence Spectroscopy Reliably Determines Galectin-Ligand Interactions. *Sci. Rep.* **2019**, *9*, No. 11851.
(33) Bakar, K. A.; Feroz, S. R. A Critical View on the Analysis of Fluorescence Quenching Data for Determining Ligand−Protein Binding Affinity. *Spectrochim. Acta, Part A* **2019**, *223*, No. 117337.
(34) Notredame, C.; Higgins, D. G.; Heringa, J. T-Coffee: A Novel Method for Fast and Accurate Multiple Sequence Alignment. *J. Mol. Biol.* **2000**, *302*, 205−217.
(35) Drozdetskiy, A.; Cole, C.; Procter, J.; Barton, G. J. JPred4: A Protein Secondary Structure Prediction Server. *Nucleic Acids Res.* **2015**, *43*, W389−W394.
(36) Yachdav, G.; Kloppmann, E.; Kajan, L.; Hecht, M.; Goldberg, T.; Hamp, T.; Hönigschmid, P.; Schafferhans, A.; Roos, M.; Bernhofer, M.; Richter, L.; Ashkenazy, H.; Punta, M.; Schlessinger, A.; Bromberg, Y.; Schneider, R.; Vriend, G.; Sander, C.; Ben-Tal, N.; Rost, B. PredictProtein—An Open Resource for Online Prediction of Protein Structural and Functional Features. *Nucleic Acids Res.* **2014**, *42*, 337−343.
(37) Lee, P. H.; Huang, X. X.; Teh, B. T.; Ng, L. M. TSA-CRAFT: A Free Software for Automatic and Robust Thermal Shift Assay Data Analysis. *SLAS Discovery* **2019**, *24*, 606−612.
(38) Jarmoskaite, I.; Alsadhan, I.; Vaidyanathan, P. P.; Herschlag, D. How to Measure and Evaluate Binding Affinities. *eLife* **2020**, *9*, 1−34.
(39) Park, C.; Marqusee, S. Analysis of the Stability of Multimeric Proteins by Effective Δ G and Effective m -Values. *Protein Sci.* **2004**, *13*, 2553−2558.
(40) Jackson, S. E.; Fersht, A. R. Folding of Chymotrypsin Inhibitor 2.1. Evidence for a Two-State Transition. *Biochemistry* **1991**, *30*, 10428−10435.
(41) Yang, J.; Zhang, Y. I-TASSER Server: New Development for Protein Structure and Function Predictions. *Nucleic Acids Res.* **2015**, *43*, W174−W181.
(42) Pettersen, E. F.; Goddard, T. D.; Huang, C. C.; Couch, G. S.; Greenblatt, D. M.; Meng, E. C.; Ferrin, T. E. UCSF Chimera—A Visualization System for Exploratory Research and Analysis. *J. Comput. Chem.* **2004**, *25*, 1605−1612.
(43) Emsley, P.; Lohkamp, B.; Scott, W. G.; Cowtan, K. Features and Development of Coot. *Acta Crystallogr., Sect. D: Biol. Crystallogr.* **2010**, *66*, 486−501.
(44) Dolinsky, T. J.; Czodrowski, P.; Li, H.; Nielsen, J. E.; Jensen, J. H.; Klebe, G.; Baker, N. A. PDB2PQR: Expanding and Upgrading Automated Preparation of Biomolecular Structures for Molecular Simulations. *Nucleic Acids Res.* **2007**, *35*, 522−525.

https://doi.org/10.1021/acsomega.1c06872
ACS Omega 2022, 7, 12643−12653